# Persistent Energetic Electrons in Methylammonium Lead Iodide Perovskite Thin Films

Daniel Niesner,[†] Haiming Zhu,[†] Kiyoshi Miyata,[†] Prakriti P. Joshi, Tyler. J. S. Evans, Bryan. J. Kudisch, M. Tuan Trinh, Manuel Marks, and X.-Y. Zhu*

Department of Chemistry, Columbia University, New York, New York 10027, United States

S *Supporting Information*

ABSTRACT: In conventional semiconductor solar cells, carriers are extracted at the band edges and the excess electronic energy ($E*$) is lost as heat. If $E*$ is harvested, power conversion efficiency can be as high as twice the Shockley−Queisser limit. To date, materials suitable for hot carrier solar cells have not been found due to efficient electron/optical-phonon scattering in most semiconductors, but our recent experiments revealed long-lived hot carriers in single-crystal hybrid lead bromide perovskites. Here we turn to polycrystalline methylammonium lead iodide perovskite, which has emerged as the material for highly efficient solar cells. We observe energetic electrons with excess energy $\langle E*\rangle \approx 0.25$ eV above the conduction band minimum and with lifetime as long as ~100 ps, which is 2−3 orders of magnitude longer than those in conventional semiconductors. The energetic carriers also give rise to hot fluorescence emission with pseudo-electronic temperatures as high as 1900 K. These findings point to a suppression of hot carrier scattering with optical phonons in methylammonium lead iodide perovskite. We address mechanistic origins of this suppression and, in particular, the correlation of this suppression with dynamic disorder. We discuss potential harvesting of energetic carriers for solar energy conversion.
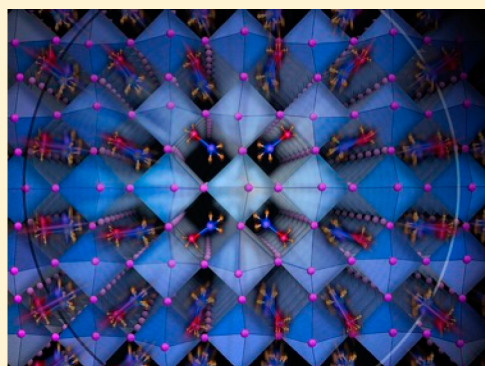
1. INTRODUCTION

The loss of excess electronic energy ($E*$) as heat in conventional semiconductor solar cells is partially responsible for the Shockley−Queisser limit of ~33% in power conversion efficiency (η).[1] If $E*$ is harvested, η can be as high as 66% in the so-called hot carrier solar cell.[2−4] However, the search for hot carrier absorbers has not been successful because $E*$ is typically lost to longitudinal optical (LO) phonons within 1 ps in most semiconductors.[5] Take GaAs as an example.[6] For electronic temperatures (kT_e) above the LO-phonon energy of 36 meV, the electronic energy loss rate $\langle dE/dt\rangle$ is on the order of 1 eV/ps. $\langle dE/dt\rangle$ is slowed down only when $E*$ is well below the energy of LO-phonons and scattering with acoustic phonons due to the deformation potential becomes dominant. In the case of GaAs at $kT_e < 10$ meV, the hot electron cooling rate decreases by 3−4 orders of magnitude to $\langle dE/dt\rangle \approx 0.1$ meV/ps at $kT_e = 4$ meV. At higher excess energies, hot electron cooling is only slowed down by the so-called "phonon bottleneck" at high excitation densities when hot LO-phonons are not cooled down fast enough and reheat the electrons,[7,8] as seen for $CH_3NH_3PbI_3$ thin films at high excitation densities ($\geq 10^{18}$/cm^3).[9−11]

The so-called Fröhlich scattering of electrons with polar LO-phonons results from the ubiquitous Coulomb potential.[5,6] For hot electrons above the LO-phonon energy in a polar semiconductor and at low excitation densities, this scattering rate can be reduced when the Coulomb potential is dynamically screened on the time scale of scattering. This intriguing possibility was demonstrated recently in hybrid lead bromide perovskites, $APbBr_3$ (A = $CH_3NH_3^+$ or $CH(CH2)_2^+$).[12] We found that long-lived hot fluorescence emission from energetic carriers with ~100 ps lifetimes in $CH_3NH_3PbBr_3$ or $CH(NH_2)_2PbBr_3$, but not in $CsPbBr_3$ at room temperature. The hot fluorescence is correlated with liquid-like dynamic responses observed in optical Kerr-effect spectroscopy, suggesting that energetic carriers are screened on time scales competitive with LO-phonon scattering. Hybrid lead bromide perovskites are not suitable for solar energy harvesting due to the large bandgap, but their iodide counterparts, in particular methylammonium lead iodide perovskite ($CH_3NH_3PbI_3$) polycrystalline thin films, are the materials of choice for efficient solar cells.[13−16] Here we probe hot electron cooling dynamics using time-resolved two-photon photoelectron (TR-2PPE) and photoluminescence (PL) spectroscopies. For photoexcitation with excess energy of ~1 eV above the bandgap, we find that energetic electrons cool down initially with a time constant of 0.28 ± 0.05 ps, but the cooling rate decreases drastically with time. The slowed cooling leaves excess electron energy $\langle E*\rangle \approx 0.25$ eV above the conduction band minimum (CBM) on the time scale of ~100 ps and with an energy relaxation rate as low as 0.3−0.5 meV/ps. We detect hot fluorescence emission from the energetic carriers, with pseudo-electronic temperatures as high as 1900 K. Contrary to

the hot "phonon bottleneck" in which hot carrier lifetime increases with excitation density, as seen for $CH_3NH_3PbI_3$ thin films at high excitation densities ($\geq 10^{18}/cm^3$),[9-11] we observe a decrease in electronic temperature with increasing density at low excitation densities ($10^{16}-10^{17}$ cm^{-3}), and we take this as an indication for screening as being responsible for reduced cooling by LO-phonons. The slow cooling rate of energetic electrons observed here for polycrystalline $CH_3NH_3PbI_3$ thin films is in excellent agreement with that in hybrid lead bromide single crystals;[12] both are $\sim 10^3$ times slower than those in conventional semiconductors,[5,6] thus suggesting the intriguing possibility of building hot carrier solar cells from hybrid lead halide perovskites.

2. EXPERIMENTAL SECTION

We grew thin films of $CH_3NH_3PbI_3$ perovskite with a thickness of 35 nm onto native-oxide terminated Si(111), in situ cleaved PbSe, or crystalline sapphire substrates in high vacuum (base pressure <10^{-6} Pa) by coevaporation of $PbCl_2$ and methylammonium iodide,[15] as detailed previously[17] and in Supporting Information. The vapor deposition process gave highly crystalline thin films with the c-axis oriented along the surface normal, with no measurable PbI_2 impurities, as confirmed by X-ray diffraction (see Supporting Information, Figure S1). Atomic force microscopy imaging (Figure S2) revealed perovskite crystallites with random lateral orientation on SiO_2 but rectangular and aligned crystallites on PbSe(001). Optical absorption spectrum (Figure S3) showed the known direct optical gap at 1.63 ± 0.01 eV, in agreement with previous reports.[18,19] Transport measurements based on photoconductivity and Hall effect revealed little charge carrier trapping in these vapor grown $CH_3NH_3PbI_3$ thin films.[20]

The freshly grown $CH_3NH_3PbI_3$ perovskite thin films were transferred in situ to an ultrahigh vacuum chamber (base pressure $\sim 10^{-8}$ Pa) for characterization by angle-resolved photoemission spectroscopy (ARPES) and TR-2PPE spectroscopy. We carry out ARPES measurement using He−I ($h\nu$ = 21.2 eV) radiation from a helium discharge lamp and a hemispherical electron energy analyzer equipped with a 2D delay line detector (SPECS Phoibos-100). The energy and angular resolutions of the analyzer were set at 40 meV and 0.2°, respectively. A bias voltage of −1.0 V was applied to the sample during ARPES measurement. The sample temperature was 190 K, as controlled by liquid nitrogen cooling and resistive heating.

We carried out TR-2PPE measurements using the same electron energy analyzer as used for ARPES. The second harmonics of two noncollinear optical parametric amplifiers (NOPAs) served as pump and probe laser pulses. The NOPAs were pumped by the second and third harmonic of a Yb-doped fiber laser (Clark-MXR Impulse) operated at 760 kHz. The center wavelengths of the visible pump and UV probe pulses were in the range of 450−465 nm or 520−530 nm and 262−300 nm, respectively. Pulse energies were typically 3 nJ and 0.3 nJ for the pump and probe, respectively. The two lasers were focused on the sample surface at 45° from surface normal to spot sizes of 250−280 μm, as determined by the knife-edge method. The temporal width of the cross-correlation traces was ∼250 fs (full width at half-maximum). We carried out all TR-2PPE measurements at temperatures of 190 and 90 K to minimize loss of methylamine and sample damage due to laser heating. At these sample temperatures, there was negligible change to 2PPE spectra with measurement time (hours). For comparison, measurements carried out at room temperature (≥295 K) showed sample degradation on the tens of minutes to hour(s) time scale under laser irradiation, in agreement with the observed degradation of $CH_3NH_3PbI_3$ nanowires at similar laser excitation densities and in room temperature lasing experiments without cooling.[21]

The vapor grown $CH_3NH_3PbI_3$ perovskite thin films were transferred through air to a vacuum cryostat (base pressure 10^{-4} Pa) for PL measurements. We recorded time-resolved PL spectra using a home-built setup based on an inverted microscope (Olympus, IX73). The excitation light of different wavelengths was generated from a regenerative amplifier (Coherent RegA amplifier seeded by Coherent Mira oscillator, 100 fs) and optical parameter amplifier (Coherent OPA 9450). The excitation light, after passing through a lens and a 50×, NA = 0.5, objective, was expanded onto the sample surface (with beam diameter ∼30 μm), and the emission light was collected by the same objective, sent through a monochromator (Newport Cornerstone 130), and focused onto a single-photon avalanche photodiode detector (IDQ, id100-50). We collected TR-PL decay kinetic traces for each wavelength (600−825 nm, 3 nm interval) using a time-correlated single photon counting module (B&H, SPC130) and reconstructed time-resolved PL spectra after correcting the system collection efficiency at each wavelength with a calibrated quartz tungsten halogen lamp. We determined the instrument response function (IRF) of the whole system by collecting scattered pump light, and the full width at hall maximum (fwhm) of IRF was determined to be 90 ps. This gave an effective time resolution of ∼20 ps.

3. RESULTS

3.1. Electronic Structure of the $CH_3NH_3PbI_3$ Thin Film.
We use a combination of ARPES and TR-2PPE spectroscopy to determine the energetic positions of the valence and conduction band edges, respectively, as illustrated in Figure 1C. ARPES of $CH_3NH_3PbI_3$ on SiO_2/Si, Figure 1A, reveals

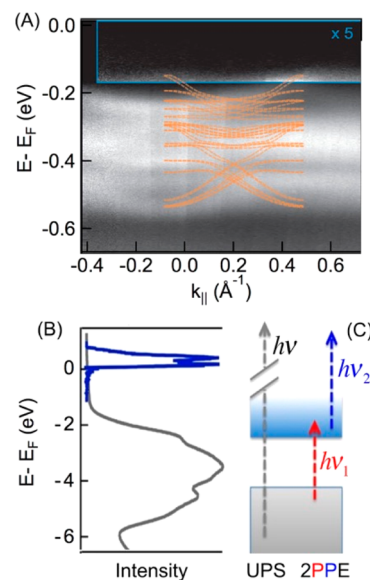**Figure 1.** Valence band structure from photoemission. (A) 2D gray scale (intensity) of ARPES ($h\nu$ = 21.2 eV) from $CH_3NH_3PbI_3$/SiO_2. Intensity in the blue box is multiplied by a factor of 5. The orange curves are reproduced from band structure calculations in ref 22. (B) Angle-integrated spectrum (gray curve) in the valence region, along with a two-photon photoemission spectrum (blue, $h\nu_1$ = 2.68 eV; $h\nu_2$ = 4.43 eV). (C) Schematics of one photon photoemission spectroscopy (UPS, $h\nu$ = 21.2 eV) and two-photon photoemission spectroscopy (2PPE).

dispersion of valence bands, consistent with the oriented nature (c-axis along surface normal) of the polycrystalline thin films. The alignment of ARPES data with the calculated band structures[22] (orange curves) allows us to determine the valence band maximum (VBM) at −1.55 ± 0.10 eV (referenced to the Fermi level, E_F). The angle-integrated ARPES spectrum, also called ultraviolet photoemission spectrum (UPS) (gray curves in Figure 1B), is in excellent agreement with previous photoemission measurements.[23,24] The 2PPE spectrum (see below) for this sample gives a conduction band minimum (CBM) at 0.00 ± 0.05 eV. Our measurements give a bandgap
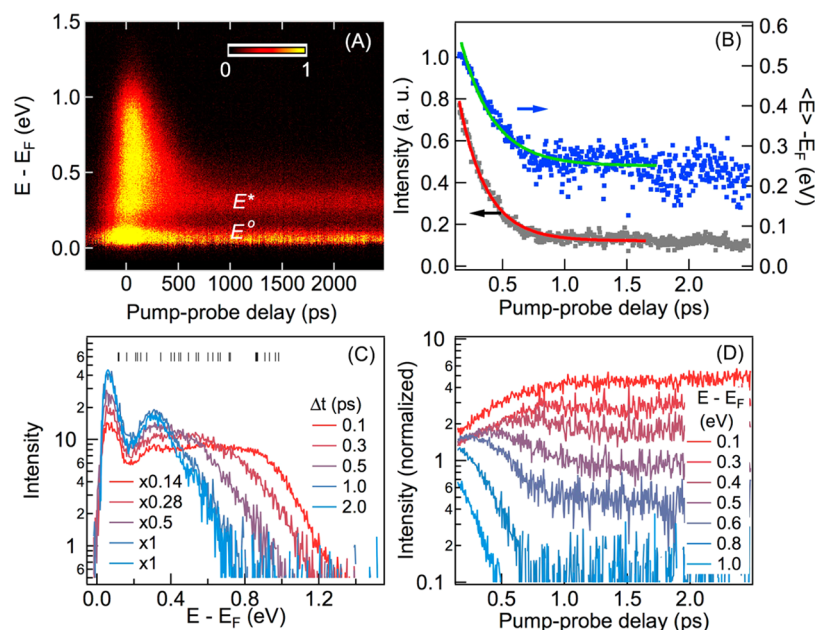
Figure 2. Initial electron cooling dynamics on the picosecond time scale. (A) Pseudocolor plot (intensity) of TR-2PPE spectra as a function of energy (above E_F) and pump−probe delay (Δt) for $CH_3NH_3PbI_3$ thin films (35 nm) on $SiO_2/Si(111)$. (B) Energy integrated photoelectron intensity (gray dots, left axis) and average electron energy of the high energy E^* 2PPE peak (blue dots, right axis) as a function of pump−probe delay. The red and green curves are single exponential fits with time constant $\tau_C = 0.28 \pm 0.05$ ps. (C) Intensity normalized TR-2PPE spectra at the selected pump−probe delays (0.1−2.0 ps). The black sticks above the spectra are theoretical predicted positions of photoelectrons (see Figure S6). (D) Kinetic profiles of normalized intensity at the indicated electron energies (from top to bottom, 0.1−1.0 eV). The pump and probe photon energies are $h\nu_1 = 2.68$ eV and $h\nu_2 = 4.43$ eV, respectively. The laser pulse energy densities are $5.4 \pm 0.5\ \mu J/cm^2$ for the pump (excitation density $1 \times 10^{18}\ cm^{-3}$) and $0.54 \pm 0.05\ \mu J/cm^2$ for probe. All measurements were carried out at sample temperatures of 190 K. On the short time scale when the pump and probe pulses overlap (−100 to 100 fs), there is contribution to 2PPE signal from UV pump and visible probe. To minimize this interference, we analyze data only at $\Delta t \geq 100$ fs.

of $E_g = 1.55 \pm 0.10$ eV, in agreement with the optical gap (Figure S3). We find that the vacuum deposition process results in $CH_3NH_3PbI_3$ thin films with different levels of n-type doping and work function, with the position of the CBM varying from ~0.00 to ~0.15 eV (see Figures S4 for comparison of samples).

3.2. Initial Cooling of Energetic Electrons (<1 ps). We probe the dynamics of photoexcited electrons using TR-2PPE. In this approach (illustrated in Figure 1C), electrons are excited across the band gap by the first laser pulse ($h\nu_1$) and, after a controlled time delay, extracted from the conduction band by the second laser pulse ($h\nu_2$). Photoelectrons are detected with energy and momentum resolution. Figure 2A shows a 2D representation of 2PPE spectra: normalized intensity (color) vs electron energy (referenced to E_F) and pump−probe delay (Δt) for the $CH_3NH_3PbI_3$ thin film on SiO_2/Si. The CBM of this sample is close to the Fermi level. Initial photon absorption creates a broad distribution of excited electrons with energies extending to 1.1 eV above CBM. We can obtain electron energies in CBM from vertical transitions at 2.68 eV (sticks on top of the spectra in Figure 2C, see Figure S6 for details) using calculated band structure along the direction of the surface normal,[25] in excellent agreement with experimental TR-2PPE spectrum at $\Delta t = 0.1$ ps. Note that all 2PPE spectra presented here correspond to pump-induced changes, that is, with background signal at negative time-delay subtracted. Due to the high laser repetition rate (760 kHz) and long carrier lifetime (~10^2 ns), there is a steady-state accumulation of electron population at the CBM (see Figure S5 for 2PPE spectra without background subtraction). In the presence of pump light, scattering between thermalized electrons at the

CBM and photoexcited ones may lead to increased population and electronic temperature just above the CBM.

The excited electrons within the initial broad distribution relax in <1 ps, as most evident in Figure 2B, which shows the average energy (blue dots) of the high energy electron peak (E^*) as a function of pump−probe delay. The relaxation dynamics clearly features two regions: the initial fast decay from $\langle E^* \rangle \approx 0.55$ eV, which can be approximately fit by a single exponential decay (green curve) with a time constant of $\tau_C = 0.28 \pm 0.05$ ps. Beyond this initial decay, the energetic electrons retain an excess energy of $\langle E^* \rangle \approx 0.25$ eV on longer time scales. The total photoemission yield (gray dots) decreases by 1 order of magnitude on the same time, as shown by the single exponential fit (red curve) with the same lifetime of $\tau_C = 0.25 \pm 0.05$ ps. Photophysical studies have shown that populations of photoexcited electrons and holes in hybrid perovskite decay on much longer time scales (>1 ns).[18,26] For $\Delta t < 2.5$ ps in Figure 2B, the photoexcited carrier populations should remain constant. The order-of-magnitude decay in intensity must be attributed to a decrease in photoionization cross section, suggesting that the physical nature of the charge carrier might be changing on the 0.25 ps time scale.

We can remove the time-dependent change in photoionization cross section in this short time window by normalizing each 2PPE spectrum by the total 2PPE intensity. The normalized 2PPE spectra, Figure 2C, reveal that the initial energy relaxation dynamics are characterized by the gradual transfer of population of higher energy states to lower ones. For $\Delta t \geq 1$ ps, further changes to both high-energy (E^*) and near CBM (E°) electron distributions are much slower, as we will focus on later in Figure 3. Another way of visualizing energy
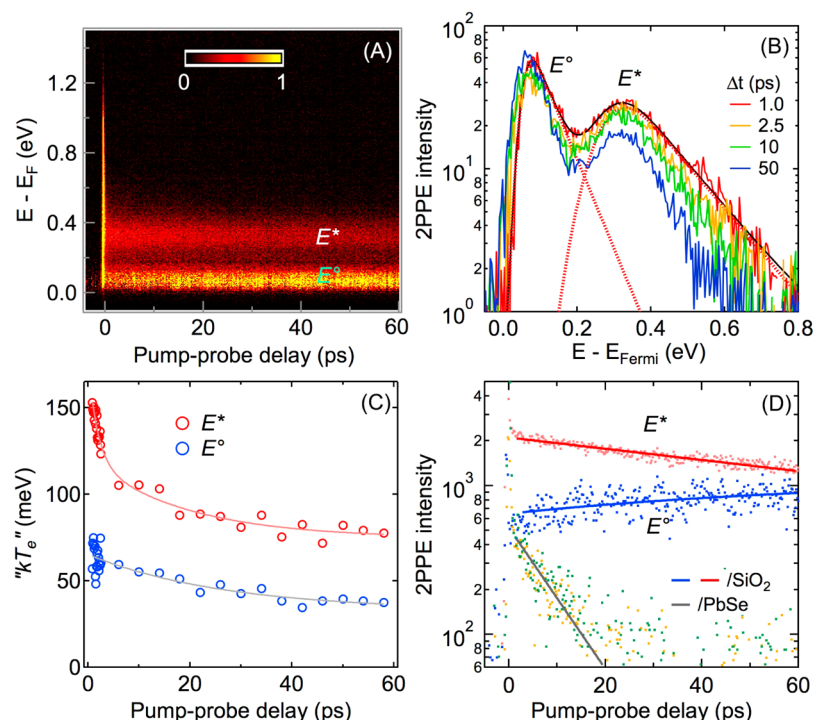
Figure 3. Slow cooling of energetic electrons. (A) Pseudocolor plot of TR-2PPE spectra for a $CH_3NH_3PbI_3$ thin films (35 nm) on SiO_2/Si(111). (B) Vertical cuts of the 2D plot at selected pump−probe delays (1, 2.5, 10, 50 ps). The solid black curve is fit to the spectrum at $\Delta t = 1.0$ ps, and the red-dashed curves are the two components of the fit. (C) Pseudo-electronic temperatures (open circles) for the high energy peak (E^*) and that near CBM ($E°$) as a function of pump−probe delay. The solid curves are double-exponential (red) and single-exponential (blue) fits, respectively. (D) Integrated 2PPE intensities from panel A for the E^* (red dots) and $E°$ (blue dots) peaks, along with single exponential fits (solid lines) with lifetime of $\tau = 110 \pm 20$ ps. The orange ($E°$) and green (E^*) dots are integrated intensities from a $CH_3NH_3PbI_3$ thin film (40 nm) on PbSe(001). The intensity from E^* is scaled to match that from $E°$. The intensities from both peaks at $\Delta t \leq 10$ ps can be fit by single exponential decay (gray line) with a lifetime of $\tau = 8 \pm 2$ ps. All measurements were carried out at sample temperatures of 190 K.

relaxation dynamics is to take horizontal cuts of the 2D plot in Figure 2A. After normalization, each time profile in Figure 2D represents relative population rise and decay dynamics at a specific electron energy. At the high-energy end (1.0 eV), we see only a simple exponential decay, with a time constant of ∼0.1 ps. At lower electron energies, we also see rising components at shorter times. The rising components extend to longer times at lower electron energies, as expected from transfer of populations from higher electron energies to lower ones being a cascading process. At the lower energy end (0.1 eV) near the CBM, we only see a rise in electron population with time.

The TR-2PPE results in Figure 2 represent a direct time-domain view of the initial electron relaxation dynamics following optical excitation, in excellent agreement with other indirect spectroscopic measurements.[10,11,27,28] At the excitation density ($\sim 1 \times 10^{18}$ cm^{-3}) used here, transient absorption studies[9,10,27] reported carrier relaxation time constants of ∼0.25 ps, which is identical to τ_C measured here. Time-resolved photoluminescence (PL) measurements[11,28] also showed subpicosecond carrier cooling time. However, unlike the hot-phonon bottleneck observed only at high excitation densities ($>1 \times 10^{18}$ cm^{-3}),[9−11] our direct measurement by TR-2PPE in Figure 1 reveals that there exist long-lived-energetic electrons, with average energy ∼0.25 eV above CBM and with lifetime ≫1 ps at low excitation densities ($\leq 1 \times 10^{18}$ cm^{-3}), in agreement with observation on hybrid lead bromide perovskite single crystals.[12] We now turn to the slow cooling of energetic electrons with remaining excess energy.

3.3. Slow Cooling of Energetic Electrons on the 100 ps Time Scale. The energetic electron distribution persists in the entire time window ($\Delta t \leq 60$ ps) probed in our experiment, as shown by TR-2PPE spectra in Figure 3A. Vertical cuts at selected pump−probe delays ($\Delta t = 1$, 2.5, 10, and 50 ps, Figure 3B) give electron energy distributions. For each spectrum at a particular Δt, we separate the high-energy electron distribution (E^*) from the quasi-thermalized electrons at the CBM ($E°$), as illustrated by the two red-dashed curves in Figure 3B for $\Delta t = 1$ ps. Here, each fit function is a Gaussian convoluted by an exponential function, $\exp[(E - \text{CBM}/(k_B T_e))]$. This spectral shape is qualitatively reproduced by calculations at the HSE[29] and the GW[30] level including spin−orbit coupling. These calculations show a discrete peak in the DOS close to the CBM, followed by a local minimum before the DOS increases steeply at 0.2 and 0.45 eV above the first peak in the cubic and tetragonal phases, respectively. Fits of the calculated DOS, which is well parametrized by a series of Gaussian peaks, to the 2PPE data are given in Figures S7 and S8. The results are consistent with the ones presented in the main manuscript based on our phenomenological DOS consisting of two peaks. While the total electron distribution is clearly not thermalized, the exponential nature of each of the two peaks on the high-energy side agrees with a Maxwell−Boltzmann-like distribution with a pseudo-electronic temperature, "T_e", shown in Figure 3C as a function of pump−probe delay. The lower energy electron distribution starts at $kT_e° = 60 \pm 10$ meV at ∼1 ps, and its cooling can be described by an exponential function (blue curve) with a time constant of 23 ± 5 ps. The relaxation of the
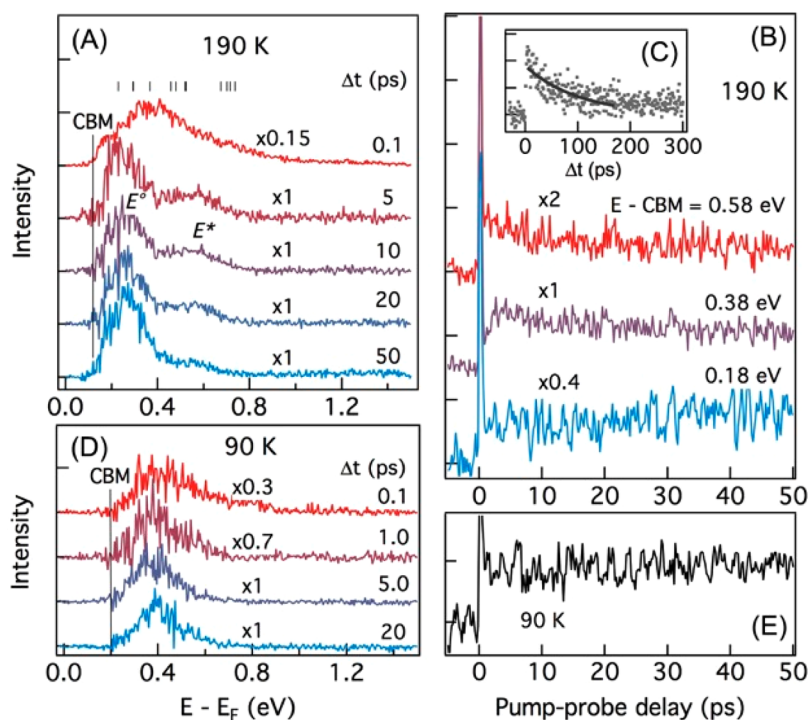
Figure 4. Comparison of electron cooling dynamics in tetragonal and orthorhombic phases for $CH_3NH_3PbI_3$. (A) TR-2PPE spectra at the indicated pump−probe delays (from top to bottom, Δt = 0.1, 5, 10, 20, and 50 ps) for a $CH_3NH_3PbI_3$ thin film (35 nm) on $SiO_2/Si(111)$ at 190 K. The CBM is at 0.12 ± 0.01 eV above E_F for this sample. (B) 2PPE intensity as a function of Δt for the indicated energies (above CBM) from the measurement at 190 K. (C) 2PPE intensity (dots) as a function of Δt at E − CBM = 0.3 eV for the measurement at 190 K. The solid curve is an exponential fit, which gives a time constant of 100 ± 20 ps. (D) TR-2PPE spectra at the indicated pump−probe delays (from top to bottom, Δt = 0.1, 1.0, 5.0, and 20 ps) for the same sample as in panel A but at a sample temperature of 90 K. (E) 2PPE intensity as a function of Δt at E − CBM = 0.2 eV from the measurement at 90 K.

high-energy distribution, with kT_e^* = 153 ± 10 meV at 1 ps, can be fit by a biexponential function (red curve) with equal contributions from a fast component of τ_1 = 2.7 ± 0.5 ps and a slower one of τ_2 = 100 ± 20 ps. The average energy cooling rate between 10 and 60 ps is 0.5 meV/ps. This cooling rate is similar to that in hybrid lead bromide single crystals probed by time-resolved fluorescence.[12] Another view of electron relaxation dynamics is shown in Figure 3D, where the integrated intensities (dots) in the regions of E^* (red) and $E°$ (blue), respectively, are plotted as a function of Δt. The decay in E^* population corresponds to the rise in the $E°$ population with a lifetime of τ_{e^*-e} = 110 ± 20 ps (single-exponential fits as solid blue and red lines). The decay in CBM population is not observed on the time scale shown here, as band edge carriers are much longer-lived (>1 ns) in hybrid lead iodide perovskites.[18,26]

The excited electron lifetime is much shorter for the $CH_3NH_3PbI_3$ thin film on the PbSe substrate (with a narrow bandgap of 0.26 eV[31]) as compared to that on SiO_2, Figure 3D. The lifetimes of both $E°$ (orange dots) and E^* (green dots) are decreased to τ = 8 ± 2 ps on the PbSe substrate, suggesting efficient diffusive transport of electrons through the $CH_3NH_3PbI_3$ thin film and transfer to PbSe at the interface (see Figure S4 for TR-2PPE spectra from hybrid perovskites on PbSe).

The above results are for hybrid perovskite in the room temperature tetragonal phase (160−315 K).[32] In a previous report, we demonstrated that the presence of long-lived hot photoluminescence from $APbBr_3$ (A = $CH_3NH_3^+$ or $CH(NH_2)_2^+$) is correlated with the liquid-like polarization

environment in the tetragonal or cubic phases, but not in the low-temperature orthorhombic phase with much suppressed dynamic disorder.[12] We now compare the energetic electron cooling dynamics in the tetragonal and orthorhombic phases for the $CH_3NH_3PbI_3$ thin film. Figure 4A shows a set of TR-2PPE spectra taken with $h\nu_1$ = 2.31 eV and $h\nu_2$ = 4.68 eV at 190 K for a $CH_3NH_3PbI_3/SiO_2$ sample. The CBM of this sample is at 0.1 eV. The excitation photon energy in Figure 4 is lower than that used in Figure 2 or Figure 3, and, as a result we observe a narrower distribution of the initially excited electrons (Δt = 0.1 ps), in agreement with prediction by the optical transitions (sticks above the 2PPE spectra, see Figure S6). Similar to the results in Figures 2 and 3, the initial electron distribution in Figure 4A relaxes on the picosecond time scale to two features, one close to the CBM (E) and a high-energy one (E^*) at ~0.3 eV above CBM. Selected kinetic profiles in Figure 3B (≤50 ps) show the monotonic population decay at higher energy (red, 0.58 eV above CBM), a fast picosecond rise followed by monotonic decay at intermediate energy (purple, 0.38 eV above CBM), and monotonic rise at lower energy (blue, 0.18 eV above CBM). The kinetic profile (gray dots in Figure 4C) for the high-energy peak at ~0.3 eV on a longer time scale (0−300 ps) can be described by a single exponential fit (black curve), with a time constant of 100 ± 20 ps.

When the same sample is cooled down to the orthorhombic phase at 90 K, we find that the CBM is shifted up by 0.08 to 0.2 eV above E_F. Except for the slight cooling on the subpicosecond time scale, the 2PPE spectrum features a single peak, with no change in peak shape for $\Delta t \geq 1$ ps. Kinetic profiles at the peak position, Figure 3E, also show nearly constant intensity within
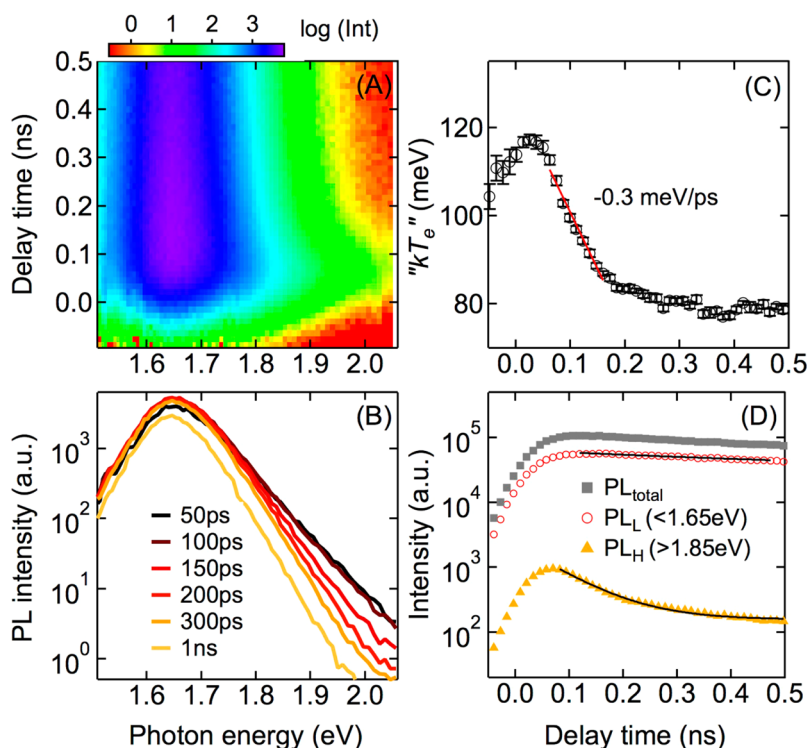
Figure 5. Hot photoluminescence from energetic carriers in $CH_3NH_3PbI_3$. (A) Pseudocolor (logarithmic intensity) plot of TR-PL spectra for a $CH_3NH_3PbI_3$ thin film (35 nm thickness) on sapphire, at $h\nu_1$ = 2.48 eV and an excitation energy density of 3.5 μJ·cm^{-2}. (B) PL spectra (horizontal cuts from panel A) at the indicated delay times (50 ps to 1 ns). (C) Pseudo-electronic temperature (kT_e, open squares) obtained from the slope of high energy tail in each PL spectrum as a function of delay time. The red line is a linear fit to the fast decay section, which gives a slope of -0.30 ± 0.05 meV/ps. (D) Integrated PL intensities: total (gray squares), $h\nu$ < 1.65 eV (red circles), and $h\nu$ > 1.85 eV (yellow triangles). The solid curves are exponential fits. The sample temperature was 294 K during measurements.

the 50 ps time window. The electron temperature stays around 90 meV showing no significant cooling in the observed time window (see Supporting Information, Figure S9). We conclude that there are no long-lived energetic electrons in the low-temperature orthorhombic phase.

As an additional control, we carry out TR-2PPE measurement on PbI_2. For excitation of a PbI_2 thin films at $h\nu_1$ = 2.68 eV, which is above the optical gap of ~2.5 eV,[33] TR-2PPE spectra (Figure S16) show a distinct peak at 0.95 eV (above E_F) from the CBM and a shoulder feature at ~0.7 eV attributable to the self-trapped exciton.[33] Except for the slight initial relaxation of excess electron energy within ~0.3 ps, the shape of the TR-2PPE spectrum remains constant for $\Delta t \geq 0.5$ ps, verifying the absence of energy relaxation dynamics on longer time scales.

3.4. Hot PL from Long-Lived Energetic Carriers. To establish that the persistence of excess electronic energy is not unique to the surface of the $CH_3NH_3PbI_3$ thin film due to the surface sensitivity of the 2PPE technique, we turn to time-resolved photoluminescence (TR-PL). The information depth of this technique is given by the extinction coefficient in the visible spectral range, which significantly exceeds the thickness of our thin-film samples. Figure 5A shows a pseudocolor (logarithm of intensity) plot of PL spectra from TCSPC for optical excitation at $h\nu_1$ = 2.48 eV, an excitation energy density of 3.5 μJ·cm^{-2}, and a sample temperature of 294 K, with a few PL spectra at indicated delay times shown in Figure 5B. Each TR-PL spectrum features a broad high-energy tail at early time, which is attributed to the radiative recombination of high-energy carriers. Similar to 2PPE spectra in Figure 3B, the high-energy tail in PL spectrum in the semilogarithmic plot (Figure

5B) is linear and can again be approximated by a pseudo-temperature, T_e^*, shown in Figure 5C as a function of delay time. The energetic carriers decay, mostly within the first 200 ps, with an average energy relaxation rate (from linear fit, red line) of 0.3 meV/ps, which is similar to the slow component of electron relaxation observed in TR-2PPE for the $CH_3NH_3PbI_3$ thin film (Figure 3C). We have also made similar observations from TR-PL measurement in $CH_3NH_3PbBr_3$ single crystals.[12] The shape of the PL spectrum remains almost constant for delay time ≥ 300 ps. The broad steady state PL spectrum has been attributed to vibronic coupling.[34] The slow decay of energetic carriers is also reflected in the different integrated PL decay dynamics at high (>1.85 eV, yellow triangles) and low (<1.65 eV, red circles) photon energies, Figure 3D. The former can be well described by a single exponential lifetime of τ^* = 80 $\pm$ 20 ps, which is close to the population decay constant from E^* to $E^°$ seen in TR-2PPE (Figure 2D). The PL intensity at lower photon energies (<1.65 eV) decays with a time constant >1 ns, as expected from radiative recombination of band edge carriers. Additional temperature dependent measurements show similar results at a lower temperature of 197 K (Figure S10), where $CH_3NH_3PbI_3$ perovskite remains in the tetragonal phase. Unfortunately, we are not able to carry out measurements at even lower temperatures for the orthorhombic phase due to the coexistence of both tetragonal and orthorhombic phases and the interphase energy transfer process,[35] which prohibited the quantitative extraction of pseudo-electronic temperatures.

We probe the dependence of pseudo-electronic temperatures on excitation photon energy and density. Figure 6A,B shows PL
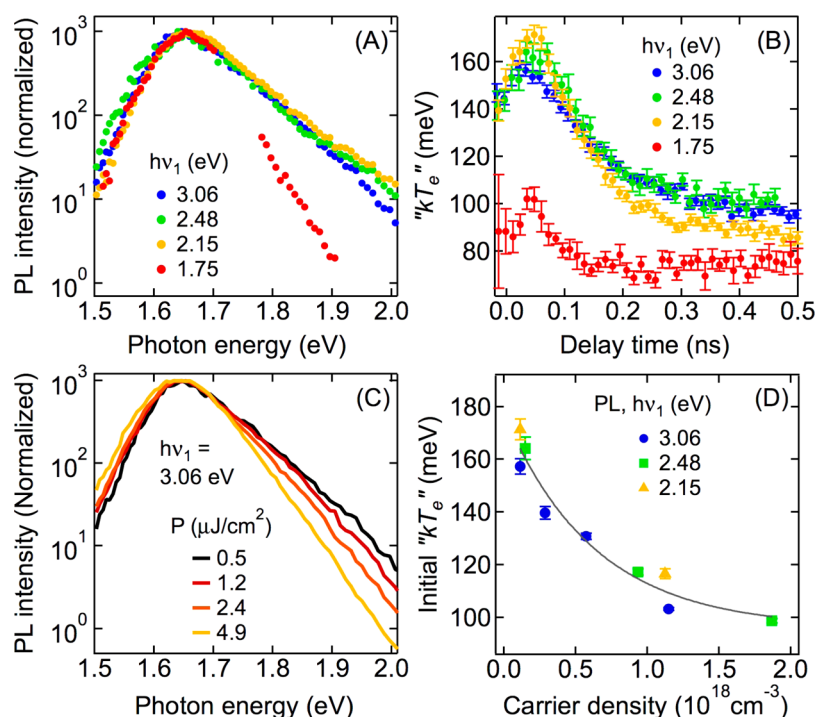
Figure 6. Dependences of hot PL on excitation photon energy and density. (A) Initial peak PL spectra (normalized) for a $CH_3NH_3PbI_3$ thin film (35 nm) on sapphire, with excitation photon energies of $h\nu_1 = 1.75-3.06$ eV and a common excitation density of $\sim 1 \times 10^{17}/cm^3$. (B) Electronic temperature (kT_e) as a function of delay time for $h\nu_1 = 1.75-3.06$ eV and a common excitation density of $\sim 1 \times 10^{17}/cm^3$. (C) Initial peak PL spectra (normalized) with an excitation photon energy of $h\nu_1 = 3.06$ eV and different pulse energy densities: $0.5-4.9$ $\mu J/cm^2$. (D) Peak electronic temperatures (kT_e) as a function of initial excitation density from PL at three excitation photon energies, $h\nu_1 = 3.06$ (blue), 2.48 (green), and 2.15 (orange) eV. The gray curve is an exponential fit to the data points.

spectra at peak electronic energy and cooling dynamics at different excitation photon energies but similar carrier density ($\sim 1 \times 10^{17}/cm^3$). For $h\nu_1 = 2.15$, 2.48, and 3.06 eV, both PL spectra and kT_e^* decay dynamics are almost the same within experimental uncertainty. The peak kT_e^* value is 0.16 eV, nearly independent of the excess excitation energies (E_{exc}, above bandgap) of $E_{exc} = 0.5$, 0.8, and 1.4 eV for $h\nu_1 = 2.15$, 2.48, and 3.06 eV, respectively. Thus, for E_{exc} exceeding 0.5 eV, part of the excess carrier energy is lost before the slow cooling process begins. When the excitation photon energy is further decreased to $h\nu_1 = 1.75$ eV, corresponding to $E_{exc} = 0.1$ eV, the initial kT_e^* decreases to 0.1 eV.

As compared to the hot phonon bottleneck effect, which leads to a positive correlation between hot carrier energy and excitation density,[9–11] our observation of long-lived energetic carriers at lower carrier densities show the opposite trend. As shown in Figure 6C for $h\nu_1 = 3.06$ eV, the high-energy tail of the PL spectra at peak carrier temperature reveals a decreasing kT_e^* with increasing excitation density. This observation is general for all excitation photon energies and excitation densities investigated, as summarized in Figure 6D (see Figures S11–S14 for power-dependent spectra and cooling dynamics at all photon energies). The inverse dependence of pseudo-electronic temperature on excitation density contradicts the two- or three-temperature model commonly used to describe free carrier thermalization. This finding supports our hypothesis of protected energetic carriers via large polaron formation, as detailed below.

4. DISCUSSION

The observation of energetic electrons with excess energy of ~ 0.25 eV and with lifetime on the ~ 100 ps time scale is unprecedented in bulk semiconductors. This is distinctly different from the hot phonon bottleneck,[7,8] seen also in $CH_3NH_3PbI_3$ thin films at high excitation densities ($\geq 10^{18}/cm^3$).[9–11] The phonon bottleneck results from the equilibration of hot carriers with the hot phonon bath that is not cooled down fast enough; in this mechanism, electronic temperature increases with increasing excitation density. In contrast, we are probing the excitation density region ($10^{16}-10^{18}/cm^3$) below the threshold for the phonon bottleneck and increasing interparticle scattering at high densities actually decreases the pseudo-electronic temperature. The latter suggests that long-lived energetic electrons observed here at low densities are in the single (quasi) particle region, and interparticle scattering actually accelerates its cooling. Before addressing the reason for the long-lived energetic electrons, we discuss the apparent differences in the energetic electron distribution from TR-2PPE and TR-PL measurements. In TR-2PPE (Figures 2-4), we observe two distributions, one near the CBM and the other described by a pseudo-electronic temperature as high as $kT_e^* = 153$ meV (at 1 ps). In TR-PL, the high-energy tail can be described by similar electronic temperature, but the two distributions are not resolvable. The difference between these two sets of data could lie in the difference in cross sections. In TR-2PPE, the high energy electron distribution could be enhanced by resonant conditions in the photoionization step (by $h\nu_2$). Hot carriers could be underestimated in PL measurement because radiative recombination cross sections from energetic carriers are lower than that from band-edge

carriers,[11] and hot PL could also be reabsorbed preferentially over band-edge PL light.[36,37]

A density-of-state (DOS) argument[38] has been used to explain the 0.4 ps population decay time constant of energetic holes,[26] and for an excess energy of 0.3 eV, this calculation predicts hot-hole lifetime reaching ~100 ps. The dispersion and DOS of the conduction band are more complex than those of the valence band because of the strong spin−orbit coupling in the constituting Pb 6p orbitals.[30] Calculations at the HSE level including spin−orbit coupling[29] show a minimum in the DOS around 0.3 eV above the CBM, in qualitative agreement with our 2PPE data, see Figure 3B. This minimum is absent in earlier calculations neglecting spin−orbit coupling.[39] The minimum in the DOS, or the maximum near the CBM, respectively, may thus be attributed to an effective reduction in dimensionality at the minimum of the spin-split band[40,41] Being broader than the LO frequency,[29] the minimum in the CB DOS can act as a bottleneck for electron−LO-phonon scattering, similar to the low DOS at the VBM.[38] This kind of bottleneck slows down the energetic relaxation of carriers at higher energies at carrier density low enough for electron−phonon scattering to be dominant over electron−electron scattering. Noteworthy, the minimum in the CB DOS is not observed to the same degree in optical spectroscopies, which typically probe the joint DOS of transitions between the CB and the VB, the latter exhibiting a monotonously increasing DOS with increasing energy of the hole[29,30] Moreover, ARPES measurements on related $(CH_3NH_3)PbBr_3$ indicate a stronger spin-splitting of the VB in the room-temperature phase than in the orthorhombic low-temperature phase,[42] in line with our 2PPE data from the CB. While this mechanism is in line with our experimental findings, it cannot explain the observed differences between the tetragonal and orthorhombic phases of $CH_3NH_3PbI_3$. The DOS argument fails similarly to account for the observation of long-lived hot carriers in single crystal hybrid $CH_3NH_3PbBr_3$ or $CH(CH_2)_2PbBr_3$ perovskite but not in the all-inorganic $CsPbBr_3$ perovskite at room temperature.[12] Note that at room temperature, $CH_3NH_3PbBr_3$ and $CH(CH2)_2^+PbBr_3$ are in the dynamically disordered cubic phase, while $CsPbBr_3$ is in the more ordered orthorhombic phase.

The correlation between long-lived energetic carriers and the presence of a high degree of dynamic disorder (e.g., in the tetragonal or cubic phase) suggests the role of screening in reducing the rate of electron−LO phonon scattering. Dynamic disorder and screening are emerging as hallmarks of lead halide perovskites that are responsible for their remarkable transport properties. Screening of a charge carrier in a polar and dynamically disordered environment can effectively reduce the scattering of a charge carrier with charged defects, with LO phonons, and with each other.[20,43,44] Zhu and Podzorov[43] proposed that such screening results in the formation of a large polaron,[45] with the size of the polarization cloud larger than the unit cell dimension. The coherent motion of the large polaron in hybrid lead halide perovskites may explain their charge carrier properties, particularly low trapping rate to defects and inverse temperature dependence in charge carrier mobility that resembles defect-free and nonpolar semiconductors.[43]

We hypothesize that large polaron formation resulting from dynamic screening may provide the necessary "protective shield" for hot electrons, thus minimizing their interaction with other high-energy phonons and drastically slowing down further cooling. The key to this "protective shield" is the reduction in Coulomb potential responsible for electron−LO

phonon scattering. The time-scale for initial electron relaxation, $\tau_C = 0.25 \pm 0.05$ ps, is consistent with the ~0.3 ps frustrated rotation (wobbling) time of the methylammonium cation[46] and is also likely the time scale for initial large polaron formation. While large polaron formation in hybrid perovskites can occur on broad time scales due to the fast motion of the methylammonium cation as well as slower motions of the lead halide framework,[44,47−50] it is the former that is competitive with the time scale for LO phonon scattering, thus leading to the partial preservation of excess electronic energy on the 100 ps time scale. In addition to reducing Coulomb potential for scattering with LO-phonons, the reduced local symmetry of a large polaron, as compared to that of the neutral lattice, can enhance Rashba splitting. Rashba splitting is one proposed mechanism behind the long carrier lifetimes in lead halide perovskites.[51−54] Calculations have shown that the interplay of spin-splitting and polaron formation gives rise to rich physics[55−59] that deviate qualitatively from the ones in the original Fröhlich model of polaron formation in the absence of spin−orbit coupling. In addition to this screening, cooperative reorientation of either organic dipoles or perhaps inorganic octahedrals can form a locally stabilized potential minimum with energetic electrons. This dynamic formation of an energetic electron sink may account for observed 3-orders of magnitude long-lived energetic electrons. This hypothesis is consistent with our earlier discovery of the correlation between long-lived hot carrier and organic cation induced liquid-like structural flexibility in $(CH_3NH_3)PbBr_3$ or $CH(CH_2)_2PbBr_3$, but not in $CsPbBr_3$.[12]

There is a dynamic competition between large polaron formation and initial energy relaxation. A "bare" electron (not dressed by the nuclear polarization) relaxes initially via efficient scattering with optical phonons and, at the same time, localizes into a large polaron. Since the initial energy relaxation rate increases with the excess energy of the electron,[5] large polaron formation may not be competitive with relaxation for very high E^* and may explain the apparent saturation of kT_e^* for $h\nu \geq$ 2.15 eV (Figure 6A,B). When the fast orientational motion of methylammonium cations is frozen in the low-temperature orthorhombic phase, the formation of large polarons is no longer competitive with cooling dynamics, and there is no evidence for slow relaxation of energetic electrons beyond ~1 ps (Figure 4D,E). Large polarons can be destabilized at high densities due to the mutual repulsion of polarization clouds.[45] Such destabilization increasingly weakens the protective large polaron shield and may explain the unusual excitation density dependence of kT_e^* (Figure 6D), which is the *opposite* of what is expected from the phonon bottleneck. Note that at high excitation densities ($>10^{18}$ cm^{-3}) the destabilization of large polarons may return the situation to more of a conventional phonon bottleneck.[9−11]

One of the spectroscopic signatures of a large polaron is absorption at three times the total energy of the large polaron.[45] The factor three gives the energy gain of only the electron, whereas the energetic cost associated with interactions within the lattice, which is twice the polaron energy, remains in the system upon photoionization. Our transient absorption measurement (Figure S17) revealed an absorption onset at ~0.23 eV, which coincides with ~3× the activation energy (75 meV) in radiative recombination reported by Savenije and co-workers.[60,61] The rapid formation of large polarons from the initial free carriers is in agreement with the absence of dispersions observed in angle-resolved TR-2PPE (Figure

S4c,d), where a large polaron should be localized to a momentum range given by the inverse of its radius. Note that ARPES in Figure 1A shows the dispersion of valence bands for free electrons, before they are subject to large polaron formation. In TR-2PPE beyond ~1 ps, localized large polarons are already formed.

The observation of slow energetic electron relaxation on the 100 ps time scale at low excitation densities ($\leq 10^{17}$/cm^3) may be relevant to E* harvesting. Our experiments demonstrate that the lower the excitation density, the more excess energy can be stored. Our 2PPE and TR-PL data recorded at excitation densities of around 10^{18} and 10^{17} cm^{-3} thus give a lower limit for the long-lived excess energy under solar flux, around 10^{16} cm^{-3}. If the excess energy stored in these protected energetic electrons can be used to do work (and assuming the same for energetic holes), we estimate that solar energy conversion efficiency can be as high as ~38% under solar radiation (see Supporting Information, Figures S18 and S19). For comparison, the Shockley−Queisser limit at the band gap of 1.55 eV is ~30%. Indeed, the observation of much decreased lifetimes of both high- and low-energy electrons for the 35 nm perovskite thin film on the low bandgap substrate of PbSe (Figure 3D) illustrates this efficient harvesting. Our findings should motivate future efforts in their efficient harvesting to realize solar energy conversion with efficiency exceeding the Shockley−Queisser limit.

5. CONCLUSION

We probe hot electron relaxation dynamics in polycrystalline CH$_3$NH$_3$PbI$_3$ perovskite thin films using time-resolved two-photon photoemission and time-resolved photoluminescence spectroscopies. We observe energetic electrons with ~0.25 eV excess energy and corresponding hot fluorescence emission on the long time scale of 100 ps, in agreement with observations on single crystal APbBr$_3$ [A = CH$_3$NH$_3$$^+$ or CH(CH$_2$)$_2$$^+$]. The lifetime of energetic carriers in hybrid lead halide perovskite is 2−3 orders of magnitude longer than those in conventional semiconductors. We attribute the suppression of carrier scattering with optical phonons to the formation of large polarons in these dynamically disordered materials.

ASSOCIATED CONTENT

⑤ Supporting Information

The Supporting Information is available free of charge on the ACS Publications website at DOI: 10.1021/jacs.6b08880.

Experimental details, additional data, additional analysis, and other control experiments (PDF)

AUTHOR INFORMATION

Corresponding Author
*Phone: 212-851-7768. E-mail: xyzhu@columbia.edu

ORCID
Daniel Niesner: 0000-0001-7810-6823
Tyler. J. S. Evans: 0000-0001-7249-508X
X.-Y. Zhu: 0000-0002-2090-8484

Author Contributions
†D.N., H.Z., and K.M. contributed equally to the work.

Notes
The authors declare no competing financial interest.

REFERENCES

(1) Shockley, W.; Queisser, H. J. *J. Appl. Phys.* **1961**, *32* (3), 510−519.
(2) Ross, R. T.; Nozik, A. J. *J. Appl. Phys.* **1982**, *53* (5), 3813−3818.
(3) Green, M. A. *Third Generation Photovoltaics*; Springer: New York, 2006.
(4) Nelson, C. A.; Monahan, N. R.; Zhu, X.-Y. *Energy Environ. Sci.* **2013**, *6*, 3508−3519.
(5) Balkan, N. *Hot Electrons in Semiconductors*; Oxford University Press: New York, 1998.
(6) Shah, J.; Leheny, R. F. *Semiconductors Probed by Ultrafast Laser Spectroscopy*; Academic: Orlando, FL, 1984; p 45.
(7) Nozik, A. J. *Annu. Rev. Phys. Chem.* **2001**, *52*, 193−231.
(8) Bockelmann, U.; Bastard, G. *Phys. Rev. B: Condens. Matter Mater. Phys.* **1990**, *42* (14), 8947−8951.
(9) Yang, Y.; Ostrowski, D. P.; France, R. M.; Zhu, K.; van de Lagemaat, J.; Luther, J. M.; Beard, M. C. *Nat. Photonics* **2016**, *10* (1), 53−59.
(10) Price, M.; Butkus, J.; Jellicoe, T.; Sadhanala, A.; Briane, A.; Halpert, J.; Broch, K.; Hodgkiss, J.; Friend, R.; Deschler, F. *Nat. Commun.* **2015**, *6*, 8420.
(11) Chen, K.; Barker, A. J.; Morgan, F. L. C.; Halpert, J. E.; Hodgkiss, J. M. *J. Phys. Chem. Lett.* **2015**, *6*, 153−158.
(12) Zhu, H.; Miyata, K.; Fu, Y.; Wang, J.; Joshi, P.; Niesner, D.; Williams, K. W.; Jin, S.; Zhu, X.-Y. *Science* **2016**, *353* (6306), 1409−1413.
(13) Lee, M. M.; Teuscher, J.; Miyasaka, T.; Murakami, T. N.; Snaith, H. J. *Science* **2012**, *338*, 643−647.
(14) Saliba, M.; Matsui, T.; Seo, J.-Y.; Domanski, K.; Correa-Baena, J.-P.; Nazeeruddin, M. K.; Zakeeruddin, S. M.; Tress, W.; Abate, A.; Hagfeldt, A.; Grätzel, M. *Energy Environ. Sci.* **2016**, *9*, 1989−1997.
(15) Liu, M.; Johnston, M. B.; Snaith, H. J. *Nature* **2013**, *501* (7467), 395−398.
(16) Burschka, J.; Pellet, N.; Moon, S.-J.; Humphry-Baker, R.; Gao, P.; Nazeeruddin, M. K.; Grätzel, M. *Nature* **2013**, *499* (7458), 316−319.
(17) Wu, X.; Trinh, M. T.; Niesner, D.; Zhu, H.; Norman, Z.; Owen, J. S.; Yaffe, O.; Kudisch, B. J.; Zhu, X. Y. *J. Am. Chem. Soc.* **2015**, *137* (5), 2089−2096.
(18) Stranks, S. D.; Eperon, G. E.; Grancini, G.; Menelaou, C.; Alcocer, M. J. P.; Leijtens, T.; Herz, L. M.; Petrozza, A.; Snaith, H. J. *Science* **2013**, *342* (6156), 341−344.

(19) D'Innocenzo, V.; Grancini, G.; Alcocer, M. J. P.; Stranks, S. D.; Lee, M. M.; Lanzani, G.; Snaith, H. J.; Petrozza, A.; Kandada, A. R. S. *Nat. Commun.* **2014**, 5, 3586.

(20) Chen, Y.; Yi, H.-T.; Wu, X.; Haroldson, R.; Gartstein, Y. N.; Rodionov, Y. I.; Tikhonov, K. S.; Zakhidov, A.; Zhu, X.-Y.; Podzorov, V. *Nat. Commun.* **2016**, 7, 12253.

(21) Fu, Y.; Zhu, H.; Schrader, A. W.; Liang, D.; Ding, Q.; Joshi, P.; Hwang, L.; Zhu, X. Y.; Jin, S. *Nano Lett.* **2016**, 16 (2), 1000−1008.

(22) Brivio, F.; Butler, K. T.; Walsh, A.; Van Schilfgaarde, M. *Phys. Rev. B: Condens. Matter Mater. Phys.* **2014**, 89 (15), 155204.

(23) Lindblad, R.; Bi, D.; Park, B.; Oscarsson, J.; Gorgoi, M.; Siegbahn, H.; Odelius, M.; Johansson, E. M. J.; Rensmo, H. *J. Phys. Chem. Lett.* **2014**, 5 (4), 648−653.

(24) Conings, B.; Baeten, L.; De Dobbelaere, C.; D'Haen, J.; Manca, J.; Boyen, H. G. *Adv. Mater.* **2014**, 26 (13), 2041−2046.

(25) Umari, P.; Mosconi, E.; De Angelis, F. *Sci. Rep.* **2014**, 4, 4467.

(26) Xing, G.; Mathews, N.; Sun, S.; Lim, S. S.; Lam, Y. M.; Grätzel, M.; Mhaisalkar, S.; Sum, T. C. *Science* **2013**, 342 (6156), 344−347.

(27) Trinh, M. T.; Wu, X.; Niesner, D.; Zhu, X. *J. Mater. Chem. A* **2015**, 3, 9285−9290.

(28) Hsu, H.-Y.; Wang, C.-Y.; Fathi, A.; Shiu, J.-W.; Chung, C.-C.; Shen, P.-S.; Guo, T.-F.; Chen, P.; Lee, Y.-P.; Diau, E. W.-G. *Angew. Chem., Int. Ed.* **2014**, 53, 9339.

(29) Demchenko, D. O.; Izyumskaya, N.; Feneberg, M.; Avrutin, V.; Özgür, Ü.; Goldhahn, R.; Morkoç, H. *Phys. Rev. B: Condens. Matter Mater. Phys.* **2016**, 94 (7), 075206.

(30) Mosconi, E.; Umari, P.; De Angelis, F. *Phys. Chem. Chem. Phys.* **2016**, 18 (39), 27158−27164.

(31) Cardona, M.; Greenaway, D. L. *Phys. Rev.* **1964**, 133 (6A), A1685−A1697.

(32) Wasylishen, R. E.; Knop, O.; Macdonald, J. B. *Solid State Commun.* **1985**, 56 (7), 581−582.

(33) Goto, T.; Maeda, J. *J. Phys. Soc. Jpn.* **1987**, 56, 3710−3714.

(34) Wehrenfennig, C.; Liu, M.; Snaith, H. J.; Johnston, M. B.; Herz, L. M. *J. Phys. Chem. Lett.* **2014**, 5 (8), 1300−1306.

(35) Wehrenfennig, C.; Liu, M.; Snaith, H. J.; Johnston, M. B.; Herz, L. M. *APL Mater.* **2014**, 2 (8), 081513.

(36) Yamada, Y.; Yamada, T.; Phuong, L. Q.; Maruyama, N.; Nishimura, H.; Wakamiya, A.; Murata, Y.; Kanemitsu, Y. *J. Am. Chem. Soc.* **2015**, 137, 10456−10459.

(37) Pazos-Outon, L. M.; et al. *Science* **2016**, 351 (6280), 1430−1434.

(38) Kawai, H.; Giorgi, G.; Marini, A.; Yamashita, K. *Nano Lett.* **2015**, 15, 3103−3108.

(39) Feng, J.; Xiao, B. *J. Phys. Chem. Lett.* **2014**, 5 (7), 1278−1282.

(40) Rashba, E. I. *Sov. Phys. Solid State* **1960**, 2, 1109−1122.

(41) Ast, C. R.; Wittich, G.; Wahl, P.; Vogelgesang, R.; Pacilé, D.; Falub, M. C.; Moreschini, L.; Papagno, M.; Grioni, M.; Kern, K. *Phys. Rev. B: Condens. Matter Mater. Phys.* **2007**, 75 (20), 201401.

(42) Niesner, D.; Wilhelm, M.; Levchuk, I.; Osvet, A.; Shrestha, S.; Batentschuk, M.; Brabec, C.; Fauster, T. *Phys. Rev. Lett.* **2016**, 117, 126401.

(43) Zhu, X.-Y.; Podzorov, V. *J. Phys. Chem. Lett.* **2015**, 6 (23), 4758−4761.

(44) Frost, J. M.; Walsh, A. *Acc. Chem. Res.* **2016**, 49, 528−535.

(45) Emin, D. *Polarons*; Cambridge University Press: Cambridge, U.K., 2013.

(46) Bakulin, A.; Selig, O.; Bakker, H. J.; Rezus, Y. L. a.; Müller, C.; Glaser, T.; Lovrincic, R.; Sun, Z.; Chen, Z.; Walsh, A.; Frost, J. M.; Jansen, T. L. C. *J. Phys. Chem. Lett.* **2015**, 6 (8), 3663−3669.

(47) Berdiyorov, G. R.; Kachmar, A.; El-mellouhi, F.; Carignano, M. A.; El-Amine Madjet, M. *J. Phys. Chem. C* **2016**, 120, 16259−16270.

(48) Even, J.; Carignano, M.; Katan, C. *Nanoscale* **2016**, 8, 6222−6236.

(49) Egger, D. A.; Rappe, A. M.; Kronik, L. *Acc. Chem. Res.* **2016**, 49, 573.

(50) Quarti, C.; Mosconi, E.; De Angelis, F. *Phys. Chem. Chem. Phys.* **2015**, 17 (14), 9394−9409.

(51) Zheng, F.; Tan, L. Z.; Liu, S.; Rappe, A. M. *Nano Lett.* **2015**, 15 (12), 7794−7800.

(52) Motta, C.; El-Mellouhi, F.; Kais, S.; Tabet, N.; Alharbi, F.; Sanvito, S. *Nat. Commun.* **2015**, 6, 7026.

(53) Etienne, T.; Mosconi, E.; De Angelis, F. *J. Phys. Chem. Lett.* **2016**, 7 (9), 1638−1645.

(54) Azarhoosh, P.; McKechnie, S.; Frost, J. M.; Walsh, A.; Van Schilfgaarde, M. *APL Mater.* **2016**, 4 (9), 091501.

(55) Jia, L.; Jing-Ling, X. *Commun. Theor. Phys.* **2006**, 46 (4), 761.

(56) Covaci, L.; Berciu, M. *Phys. Rev. Lett.* **2009**, 102 (18), 186403.

(57) Li, Z.; Covaci, L.; Berciu, M.; Baillie, D.; Marsiglio, F. *Phys. Rev. B: Condens. Matter Mater. Phys.* **2011**, 83 (19), 195104.

(58) Li, Z.; Covaci, L.; Marsiglio, F. *Phys. Rev. B: Condens. Matter Mater. Phys.* **2012**, 85 (20), 205112.

(59) Vardanyan, K. A.; Vartanian, A. L.; Kirakosyan, A. A. *Eur. Phys. J. B* **2012**, 85 (11), 367.

(60) Savenije, T. J.; Ponseca, C. S.; Kunneman, L.; Abdellah, M.; Zheng, K.; Tian, Y.; Zhu, Q.; Canton, S. E.; Scheblykin, I. G.; Pullerits, T.; Yartsev, A.; Sundström, V. *J. Phys. Chem. Lett.* **2014**, 5 (13), 2189−2194.

(61) Hutter, E. M.; Gélvez-Rueda, M. C.; Osherov, A.; Bulović, V.; Grozema, F. C.; Stranks, S. D.; Savenije, T. J. *Nat. Mater.* **2016**, DOI: 10.1038/nmat4765.